Revealing the thermal decomposition mechanism of RDX crystal by a neural network potential

Qingzhao Chu[a], Xiaoya Chang[a], Kang Ma[b], Xiaolong Fu[c], Dongping Chen[a,*]

[a] State Key Laboratory of Explosion Science and Technology, Beijing 100081, China
[b] Beijing Institute of Electronic System Engineering, Beijing, 100143, China
[c] Xi'an Modern Chemistry Research Institute, Xi'an, 710065, China.

Abstract

A neural network potential (NNP) is developed to investigate the complex reaction dynamics of RDX thermal decomposition. Our NNP model is proven to possess good computational efficiency and retain the *ab initio* accuracy, which allows the investigation of the entire decomposition process of bulk RDX crystal from an atomic perspective. A series of molecular dynamics (MD) simulations are performed on the NNP to calculate the physical and chemical properties of the RDX crystal. The results show that the NNP can accurately describe the physical properties of RDX crystal, like cell parameters and equation of state. The simulations of RDX thermal decomposition reveal that the NNP could capture the evolution of species at the *ab initio* accuracy. The complex reaction network was established, and a reaction mechanism of RDX decomposition was provided. The N-N homolysis is the dominant channel, which cannot be observed in previous DFT studies of gas RDX. In addition, the H abstraction reaction by NO_2 is found to be the critical pathway for NO and H_2O formation, while the HONO elimination is relatively weak. The NNP gives an atomic insight into the complex reaction dynamics of RDX and can be extended to investigate the reaction mechanism of novel energetic materials.

Keywords: Energetic materials; Decomposition; Neural network potential; Molecular dynamics

---

*Corresponding author: Dongping Chen, dc516@bit.edu.cn

1. Introduction

RDX (1,3,5-Trinitroperhydro-1,3,5-triazine) is a common high-energy dense oxidizer in many energetic materials (EMs), which is a representative example of the caged polynitroamines, such as HMX and CL-20[1]. RDX has been used for more than 70 years, and there is a long history of scientific research on the material[2]. Thermal decomposition is a fundamental process for any EMs exposed to external stimuli. It relates to the ignition of explosives, the subsequent detonation performance, and their sensitivity from mechanical stimuli to direct heating[3]. A comprehensive understanding of thermal decomposition mechanisms is essential for the performance and safety of EMs.

The decomposition mechanism of RDX crystal is widely investigated in abundance by experiments and computational simulations. Wight and Botcher [4] explored the initial products of RDX pyrolysis by FTIR spectrum; they found NO and N_2O_4 are the main gas-phase products in the initial stage, illustrating that the N-N bond scission is the first step in the thermal decomposition of RDX crystal. Zhao et al. [5] studied the infrared multiphoton dissociation (IRMPD) of RDX in a molecular beam using time-of-flight velocity spectra (TOFVS). They detected the major products from laser photolysis (mass range from 22 to 120 amu). It was concluded that the dominant channel in the RDX decomposition is a concerted symmetric triple fission of the ring in RDX. Khichar et al.[6] conducted thermal analysis on RDX using a coupled TGA/DSC-FTIR system. N_2O, NO_2, CH_2O, NO, HCN, CO_2, CO, and H_2O were identified as the major decomposition products. The combustion characteristics of RDX crystal were studied by Yan et al. [7] with optical diagnosis methods. The reactions of NO and HCN (the products from RDX decomposition) dominate the heat release in the flame, which are further converted to N_2, H_2O, and CO in the downstream flame. Although many efforts are made to understand the thermal decomposition of RDX, the overall chemical mechanism during thermolysis remains obscure due to the ultrafast and complex reactions involved, which can hardly be captured in experiments.

The quantum mechanics (QM) approach is employed in the investigations of the thermal decomposition of RDX molecules, especially for the initial decomposition reaction of single RDX molecule. The first theoretical analysis of the decomposition mechanism for RDX was conducted by Melius and Binkley[8] at the MP4 level of theory. They found that the N-N homolytic cleavage in an RDX molecule is the primary decomposition pathway with a dissociation energy of ~48 kcal/mol. Harris and Lammertsma[9] calculated the potential energy surface at the B3LYP/6-31G* level of theory and identified that the N-NO_2 and C-H bonds in RDX are fragile. A mechanism is proposed to initiate the decomposition by N-N bond cleavage and propagate by H atom transfer. A detailed decomposition mechanism was established by Patidar et al.[10], including HONO elimination, N-NO_2 homolysis, reactions with NO, autocatalytic decomposition via HONO and $ONNO_2$ addition, and hydrogen abstraction via NO. In this mechanism, RDX gradually decomposes into N_2O, NO_2, NO, HCN, CH_2O, CO, CO_2, H_2O, and other small gas-phase products. Recently, Zhang et al.[11] proposed a kinetic model for RDX decomposition. They claimed that the N-NO_2 homolysis to form RDR radical is the dominant decomposition pathway of RDX, which subsequently undergoes C-H β-scission and ring-opening reaction. Although the accurate DFT calculations reveal

the decomposition of RDX molecules, the current analysis is all derived from single RDX molecules and the potential intermolecular reactions in the condensed phase requires further investigation.

In the past two decades, *ab initio* molecular dynamics (AIMD) simulations were performed to investigate the initial decomposition pathways of HMX[12], CL-20[13], and NTO[14] molecules. However, these works were limited to a small system (i.e., <300 atoms), and a short reaction time (i.e., <50 ps). Despite impressive progress in computing hardware and software in recent decades, AIMD calculations on the complete reaction process of RDX crystal are still challenging due to the high computational cost. To alleviate the demand for computing power, empirical potentials (or force fields) were developed to construct the potential energy surface (PES) from DFT calculations. Such empirical potentials, including ReaxFF[15,16] and REBO[17], trade accuracy for a lower computational expense, making it possible to extend simulation scales to orders of magnitude beyond AIMD methods. ReaxFF is a bond order-based force field that describes reactive systems without prior knowledge of the predefined reactive sites. It is a powerful tool for studying kinetic mechanisms for large molecules and complex reactions[18]. However, the computational accuracy of the ReaxFF model is relatively limited due to the underlying functional forms. Recently, machine learning-based tools, especially neural networks (NNs), have been applied to construct PES models in an entirely data-driven manner, where the PES is abstracted from a well-selected training dataset using suitable functional expressions automatically[19]. NN models constitute a very flexible class of mathematical functions, enabling the development of PES models with the efficiency of the empirical potentials and the accuracy of the DFT method. A few successful NN-based potentials (NNPs) are proposed for materials and biomolecules [20,21], which can accurately reproduce the interatomic forces and energies predicted by *ab initio* calculations in condensed matters. In particular, Cao et al. [22] implemented an NNP to reveal the mechanisms of CL-20/TNT co-crystal. They found that the TNT molecules in the co-crystal act as a buffer to slow down the chain reactions triggered by nitrogen dioxide, which is more significant at lower temperatures.

In this work, we develop an NNP to explore the decomposition mechanism of RDX crystals. The NNP is first trained and validated against the DFT database with bulk RDX molecules under a wide range of thermodynamic states. The lattice constant, the equation of state, decomposition rate, and reaction pathways are calculated with the NNP to evaluate its accuracy. Finally, the decomposition mechanism of bulk RDX molecules is proposed for the first time at the *ab initio* level of accuracy.

2. Computational methods

2.1 Development of Neural network potential

The NNP is constructed following the Deep Potential (DP) scheme developed by Zhang et al. [20]. In the DP scheme, PES is represented by a deep neural network model that interprets the atomic coordination (R) into interatomic forces (F) and energies (E). The deep neural network contains a filter (embedding) network with three layers (25, 50, and 100 nodes/layer) and a fitting net with three layers (240 nodes/layer). The loss function (L) is defined as,

$$L = \frac{p_e}{N}\Delta E^2 + \frac{p_f}{3N}\sum_i |\Delta F_i|^2 \quad \#(1)$$

where p_e and p_f are the weight for the energy and force terms, respectively. N represents the number of atoms in the structure. Similar to a classical neural network, the DP scheme trains the model by computing the gradient of the loss function using the back-propagation algorithm [23]. The NNP is trained for 1.0×10^6 iterations with an exponentially decaying learning rate from 1.0×10^{-3} to 5.0×10^{-8}.

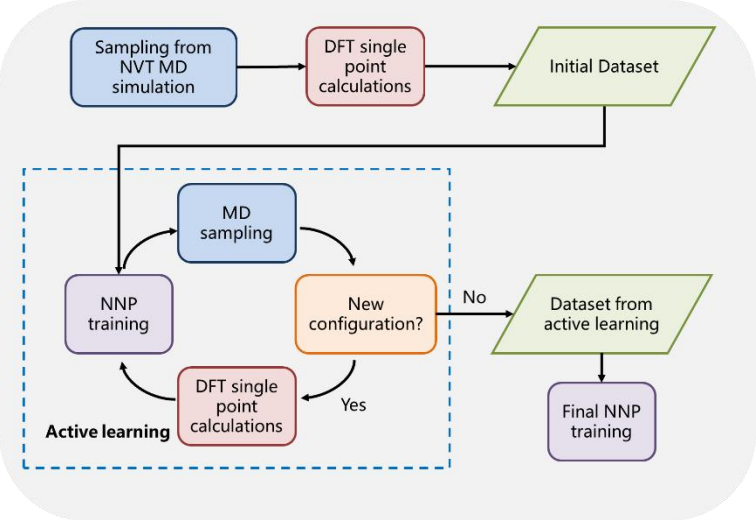

Fig. 1 Illustration of the NNP model training in the DP scheme.

The performance of NNPs highly depends on the training dataset [24–26]. Although NNs are good at interpolating between training points, they cannot predict the energies and forces of configurations away from those in the training set. Therefore, it is critical to ensure the dataset covering the PES of interest. Fig. 1 illustrates the overall training using the DP scheme. The unit cell of RDX crystal is used to prepare the training sets. A set of reactive MD simulations are performed for 40 ps to obtain trajectories under an NVT ensemble at temperatures of 300, 1000, 2000, 3000, and 4000 K using the ReaxFF forcefield[27,28]. One thousand configurations are randomly selected from the above trajectories to build the initial dataset, and high-level DFT calculations are further conducted to obtain accurate energies and forces. DFT calculations are performed using the CP2K package [29]. Core electrons are treated using Goedecker−Teter−Hutter (GTH) pseudopotentials and the Perdew Burke Ernzerhof (PBE) generalized gradient approximation method [30,31]. The Grimme DFT-D3 method [32] is used to account for dispersion interactions. A double-zeta Gaussian basis set plus polarization (DZVP-MOLOPT) [33] is considered. In addition to MD simulations, further configurations are obtained using active learning sampling implemented in the DP-GEN package [34]. In the stage of active learning, four NNPs are firstly trained with different random seeds. Then, MD simulations with a temperature range from 300 to 4000 K are performed using one of the NNPs. The MD trajectories are evaluated by the other three NNPs to obtain the deviation of atomic forces, which is used as a criterion to identify the new configurations. The configurations with relative deviation in the range of 0.05-0.15 are added to the training set. In total, we perform 20 iterations of active learning to derive an accurate NNP for the decomposition of RDX crystal (Table 1). The iterations 1-13 investigate the RDX decomposition process under an NVT ensemble with a 2x2x2 supercell. The temperature gradually increases from 300 K to 4000 K, covering the entire potential surface during RDX decomposition. In addition, we add iterations 14-20 to impose

the mechanical behaviors under compression and tension, and construct the equation of states for the RDX crystal. With the above method, the final *ab initio* NNP is trained.

Table 1 Detailed simulation setting in the active learning process of DPGEN.

Iteration	Scale factor[1,2]	MD steps	Ensemble	Temperature (K) [2]
1	1.00	1000	NVT	300, 500
2	1.00	3000		
3	1.00	5000		
4	1.00	10000		
5	1.00	1000	NVT	1000, 2000
6	1.00	5000		
7	1.00	10000		
8	1.00	1000	NVT	3000, 4000
9	1.00	5000		
10	1.00	10000		
11	1.00	40000		
12	1.00	100000		
13	1.00	400000		
14	0.96, 1.00, 1.04	5000	NVT	300, 500
15	0.96, 1.00, 1.04	10000		
16	0.88, 0.92, 1.08, 1.12	10000		
17	0.96, 1.00, 1.04	5000	NVT	3000, 4000
18	0.88, 0.92, 1.08, 1.12	10000		
19	0.88, 0.92, 0.96, 1.00, 1.04, 1.08, 1.12	10000		
20	0.88, 0.92, 0.96, 1.00, 1.04, 1.08, 1.12	10000		

[1] The coordinates of systems are transformed by the scale factors in x-, y- and z-directions.

[2] MD simulations are performed under different scale factors and temperatures respectively.

2.2 MD simulations

The RDX decomposition process is investigated with the final NNP. The simulation is performed under the NVT ensemble with a 2x2x2 supercell. The equations of motion are integrated by the velocity Verlet method using periodic boundary conditions. A Nose–Hoover thermostat is applied with an equilibrium temperature of 1000, 1250, 1500, 1750, 2000, 2250, 2500 K and a dump parameter of 20 fs. A 100-ps MD simulation is performed with a time step of 0.l fs. Three parallel simulations are performed for each NVT MD simulation to ensure the statistical significance of the simulated results. The ReacNetGenerator [35] is used to extract species and reactions from the MD trajectories.

3. Results and discussion

3.1 Accuracy and efficiency of the NNP model

The overall performance of the NN potential is tested against the *ab initio* database. Figure 2 shows the prediction of DFT energies and forces using the NNP trained by the DP scheme. The results predicted from the ReaxFF model [28] are also included for comparison. The energies predicted from the NNP cluster on the diagonal in Figure 2a suggesting the good fitting ability of the NNP. In contrast, the energies of the ReaxFF model scatter with the maximum deviation as 0.2 eV/atom. The NNP exhibits a lower mean absolute error (MAE) than the ReaxFF model (0.026 *v.s.* 0.091 eV/atom). Besides atomic energies, the NNP shows excellent force prediction performance with an MAE of 0.41 eV/Å (Figure 2a). However, the ReaxFF model predicts unphysical results against the QM values. This issue can be explained by the parameterization of ReaxFF, as only atomic energies are taken as the training targets. By considering the atomic forces in the loss function (Eq. 1), the NNP significantly improves the model prediction and thus accurately captures the dynamic evolution of the RDX decomposition process.

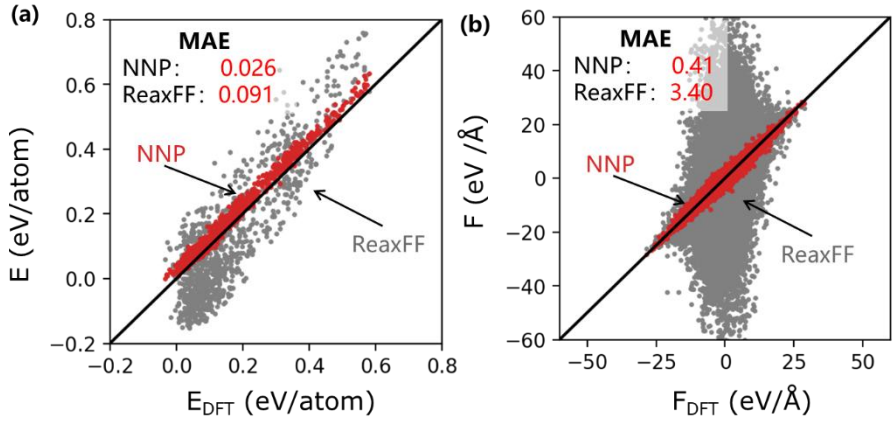

Fig. 2 Mean absolute errors of (a) atomic energy and (b) force for NNP and ReaxFF models on the *ab initio* database.

We also evaluate the computational costs of NNP, ReaxFF, and DFT methods on the bulk RDX systems with 100 to 100,000 atoms (Figure 3). The neural network potential-based molecular dynamics simulations (NNP-MDs) are performed on an NVIDIA V100 GPU. The ReaxFF and DFT calculations are solved on a 64-processor server with two AMD EPYC 7452 CPUs. The NNP shows a linear scaling rule in the computational cost, which is 27 times faster than the ReaxFF model. Compared to the AIMD method, the simulations using NNP are faster by four orders of magnitude. This significant improvement in the computational costs is consistent with previous works using the NNPs[36]. This can be attributed to the implementation in the neural network combining the-state-of art GPU computing. The computing efficiency of the NNP in small systems with hundreds of atoms deviates from other significant cases. This is expected as the implementation of the NNP is optimized for large systems. Also, it is worth noting that the ReaxFF model exhibits an O(N) scaling rule rather than an O(NlogN) scaling rule, different from previous works in the low-density gas[36]. The better performance of the NNP enables the exploration of a system with tens of thousands or even millions of atoms at the *ab initio* accuracy, providing a feasible approach to investigate the complex reaction network of RDX crystal from an atomic perspective.

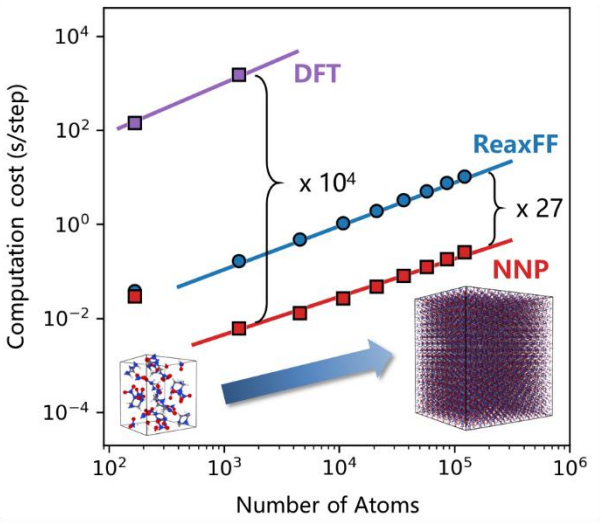

Fig. 3 Computational cost of NNP (red square), ReaxFF (blue circle), and DFT (purple square) methods on bulk RDX systems with 100 to 100,000 atoms. The insert shows snapshots of the corresponding systems (from 168 to 223,608 atoms).

3.2 Physical properties

Table 2 presents the cell parameters of α-RDX crystal predicted from DFT, NNP, and ReaxFF methods and the values from the experiments by Choi et al.[37]. As described in section 2.1, DFT calculations are performed by the PBE-D3 level of theory. In Table 2, the cell parameters calculated by PBE-D3 method are in good agreement with experiments, ensuring the excellent quality in the training dataset. The cell parameters from the NNP fall within 2% of the experimental values, and the error in the volume of unit cell is within 3%. The predicted values from the ReaxFF model are also well reproduced as the experimental values; all three cell parameters are underestimated by 2% and the volume of unit cell is smaller by 6%. This highlights that the parameterization in the ReaxFF model with atomic energy is capable of reproducing the crystallographic parameters of α-RDX crystal.

Table 2 Crystallographic parameters of α-RDX crystal calculated using DFT, NNP, and ReaxFF methods. [a]

Parameter	Experiment[37]	DFT (PBE-D3)	NNP	ReaxFF[28]
a (Å)	13.182	13.325	13.415 (0.02)	12.938 (-0.02)
b (Å)	11.574	11.614	11.462 (-0.01)	11.331 (-0.02)
c (Å)	10.709	10.807	10.960 (0.02)	10.502 (-0.02)
V (Å^3)	1633.856	1672.454	1685.233 (0.03)	1539.598 (-0.06)

[a] The values in parentheses are the percentage error deviating from experimental values.

The predictions of the equation of state (EOS) by DFT, NNP, and ReaxFF models are presented in Fig. 4. The NNP well reproduces the DFT results of the RDX crystal. It should be noted that only the central portion of the EOS curves (the rectangle region) is included in the training dataset. However, the NNP also achieves a good

agreement on structures out of the training dataset, indicating a satisfactory extrapolation performance. In comparison, the ReaxFF method fails to construct the EOS of RDX crystal and predicts an incorrect equilibrium structure. The ReaxFF overestimates the potential energies at the compression process (Volume = 5-10 Å^3/atom), which might affect the investigation of explosion or shock loading leading artificial formation of local hotspots.

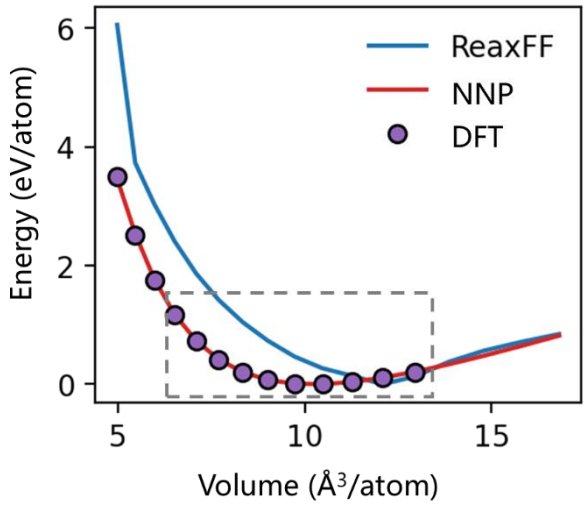

Fig. 4 Equation of state curve for RDX crystal. The blue line, red line, and purple circles denote ReaxFF, NNP, and DFT results, respectively. The dashed rectangle represents the structures included in the training sets.

3.3 Species evolution during RDX decomposition

The species evolution during RDX decomposition is calculated at 1500, 1750, 2000, 2250, and 2500 K. Figure 5 presents the evolution of RDX molecules predicted by NNP and ReaxFF models. Initially, 64 RDX molecules are packed in the supercell, and gradually decomposes in the first 10 ps. For both models, the decomposition rate of RDX increases with the temperature. The NNP predicts a higher decomposition rate than ReaxFF model at all temperatures. We also perform an AIMD simulation for RDX decomposition to validate the reaction rate seen in the NNP. Considering the calculation cost, the AIMD simulation is performed on an RDX unit cell (8 molecules) at 3000 K. As shown in Fig. S1a, the NNP reproduces the species evolution of RDX in AIMD simulations. In contrast, noticeable deviations are seen in the ReaxFF model, highlighting the importance of model accuracy to mimic the dynamic evolution in thermal decomposition.

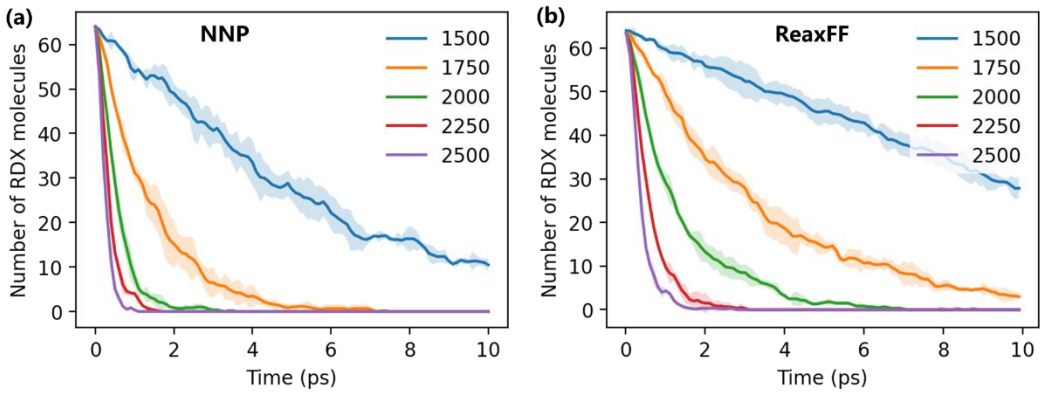

Fig. 5 Evolution of the number of RDX molecules predicted by NNP (a) and ReaxFF (b) models. The temperatures are 1500, 1750, 2000, 2250, and 2500 K. The shadow regions represent the error bars among the three simulations.

To better understand the RDX decomposition kinetics, the reaction rate constant is calculated using the first-order reaction model:

$$C(t) = C_0 \exp(-kt),$$

where C_0 is the initial number of reactants, $C(t)$ refers to the reactant number at a specific time t, and k is the rate constant. By logarithmic transformation, we can compute the rate constant of RDX decomposition using the following equation:

$$k = \ln\left(\frac{C_0}{C(t)}\right) / t.$$

The rate constants are calculated using the species evolution of RDX molecules in 10 ps. The rate constant derived from the NNP is in the same order as the ReaxFF model but higher by a factor of two. From the Arrhenius plot in Fig. 6, Arrhenius parameters for RDX decomposition are determined by a direct fitting. The activation energies predicted by NNP and ReaxFF are 25.24 and 26.01 kcal/mol, respectively. The results from both models are in good agreement with the experimental value of 28.6 kcal/mol using the Kissinger method[38]. The above discussion confirms that the NNP accurately describes the kinetics of RDX decomposition. In the following section, we discuss the detailed decomposition mechanism of RDX crystal from condensed phase into gas-phase intermediates.

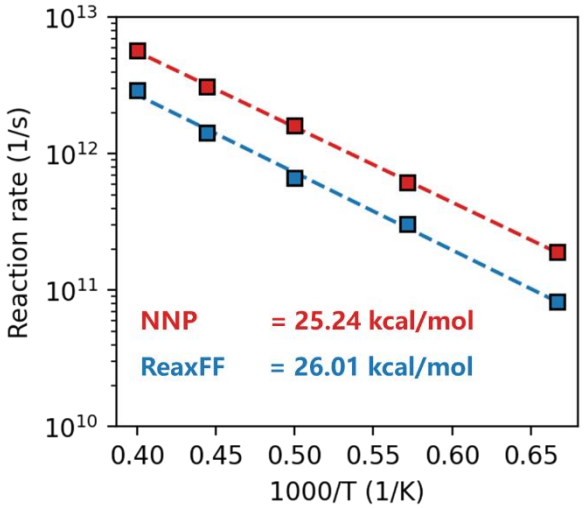

Fig. 6 Predicted activation energy for RDX decomposition by NNP (red) and ReaxFF (blue) models.

The evolution of seven key gas-phase molecules at 2500 K is presented in Figure 7. Figure 7a shows the decomposition in the first 100 ps by the NNP. During the decomposition, the first major intermediate is NO_2 produced from the homolytic fission of the N-NO_2 bond in RDX molecules. This finding is consistent with previous works[39] as the breakage of N-NO_2 bond triggers the RDX decomposition. Chakraborty et al.[39] identified the first bond-breaking event as N-NO_2 bonds in a single RDX molecule compared to the HONO elimination and concerted ring break. The corresponding dissociation energy is the lowest among the other two potential reactions

computed by the B3LYP method. The NO_2 molecules are subsequently consumed in a rapid manner within 10 ps, followed by the production of NO and H_2O molecules. In the later stage, the production of N_2 and CO_2 are observed, and the overall reactions reach an equilibrium after 100 ps. The production of NO_2, NO, HNO_2, H_2O, and CO_2 is also reported in a recent FTIR experiment[40].The RDX decomposes into NO_2, NO and H_2O first, and then NO_2 and NO starts to decrease after a certain time, while H_2O continues to increase. Although the experiments[40] are performed at a lower temperature (e.g. 538K), the product evolution agrees with our NNP simulations qualitatively. The predicted species evolution using the ReaxFF model is included in Figure 7b. The overall evolution is similar with the NNP results, where NO_2 is the major intermediate, and N_2, H_2O, and CO_2 are the major products. Compared with the results of ReaxFF model, the NNP predicts more NO molecules, a faster H_2O production rate, and a higher N_2 concentration at the equilibrium. To validate the accuracy of the NNP in species evolution, the evolution of NO_2, NO, and H_2O are also compared in Fig. S1, indicating that the NNP outperforms the ReaxFF model in the prediction of the decomposition process. In addition, the NNP predicts that N_2 is the most abundant final product, followed by H_2O and CO_2. This finding agrees with the experiments where the final products of RDX decomposition is 37% N_2, 31% H_2O, 18% CO_2, and 14% CO.[41] It should be noted that the NNP predicts a lower concentration of CO, because PBE method underestimates the stability of CO[42]. The current NNP inherits this issue to some extent, and further improvement can be carried on to add more accurate DFT calculations of CO-involved reactions in the training set.

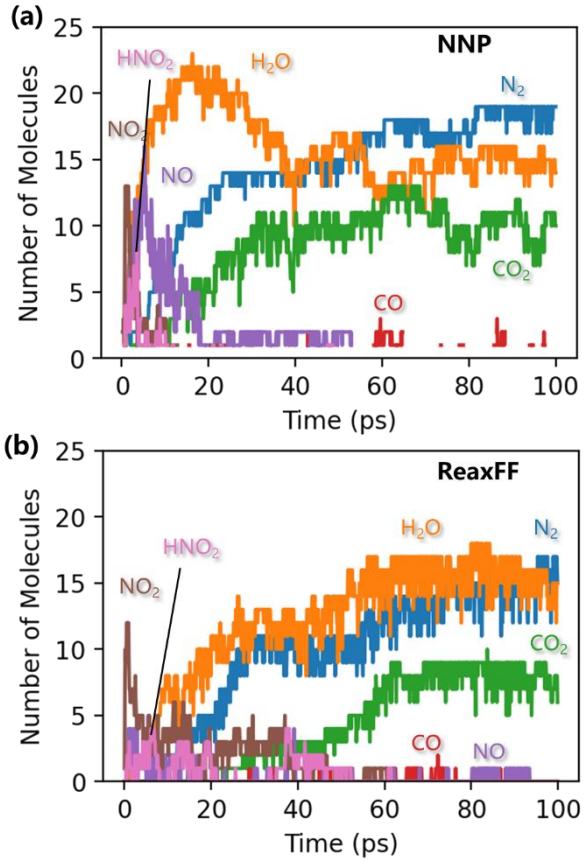

Fig. 7 Gas-phase species during RDX decomposition predicted by NNP (a) and ReaxFF (b) models.

3.4 Decomposition mechanism

The MD trajectories using the NNP are further analyzed by ReacNetGenerator [35] to reveal the complex reaction network. The primary reaction pathways of RDX decomposition and the formation of final products are constructed in Fig. 8, where the arrow width represents the observed number of reactions. The major channel of RDX decomposition starts with N-N homolysis to produce NO_2 molecules and RDR radicals, which agree with previous DFT studies[10,11]. Then, the RDR radicals mainly decompose through three pathways: (1) subsequential N-N homolysis to INT1 and NO_2 molecules, (2) ring-opening reactions to form INT2, and (3) H abstraction/addition reactions. The N-N homolysis is the primary pathway for RDX and RDR decomposition to rapidly form NO_2 molecules, corresponding to the peak of NO_2 at ~1 ps in Figure 7a. The NO_2 is a key precursor to form HNO_2; it can abstract H from molecules such as RDX, RDR, INT1, INT2, and INT3. The HNO_2 further decomposes into NO and OH radicals, corresponding to the peak of NO at ~10 ps in Fig. 7a. The OH radical undergoes H abstraction to form H_2O.

In our simulations using the NNP, the N-N homolysis is more critical compared to the ring-opening reactions and the H abstraction/addition reactions in the RDR decomposition as the corresponding frequency number is 49, 16 and 11. This finding here disagrees with the DFT calculations by Chakraborty et al.[39]; they reported that the RDR prefers to decompose through the ring-opening reactions rather than N-N homolysis. The reason might be attributed to the effects of neighbor molecules. Chakraborty et al. [39] studied the reaction dynamic of an isolated molecule. In contrast, our NNP-MD simulations resolve the decomposition of the bulk RDX crystal. The neighbor molecules around the RDR might impose intense steric effects on the ring-opening reactions prohibiting the progress of ring opening, and this effect are discussed latter. In previous DFT studies [10,39], the HONO pathway is another channel for RDX decomposition, where H atoms migrate to -NO_2 in RDX and undergoes a direct elimination of HNO_2. This pathway is observed in our NNP-MD simulations, but its frequency is very low (e.g. 2 times). Instead, majority of HNO_2 molecules is produced by the H abstraction reaction involving NO_2 (e.g. 1890 times). Such H abstraction reaction is also reported by Patidar et al.[10] and Zhang et al.[11]. Their results showed that the H abstraction by NO_2 has a much lower energy barrier than HONO elimination reactions (30.8 *v.s.* 38.3 kcal/mol). In addition to the NO_2- and HNO2-related reactions, large fragments (INT1, INT2, INT3) are identified in simulations. The INT1 undergoes a N-N homolysis and H abstraction reaction to yield TAZ, which can further decompose via a ring-opening process to form INT3. Both INT2 and INT3 are chain-like molecules; they undergo chain breakage to form small fragments such as $(CH_2)_2N$ and CH_2N_2, which yield HCN molecules in further decomposition. Finally, HCN molecules are oxidized to form N_2, CO, and CO_2. These reactions are slower and more complex than the NO_2-related reactions, resulting in the decay in N_2 and CO_2 production. In summary, the decomposition mechanism of RDX can be divided into two stages: (1) N-N homolysis to form NO_2 and HNO_2; (2) ring-opening and chain breakage reaction of large fragments. The first stage exhibits a high reaction rate and produces NO_2, NO, and H_2O. The second stage is relatively slower and more complex, resulting in the formation of N_2, CO, and CO_2.

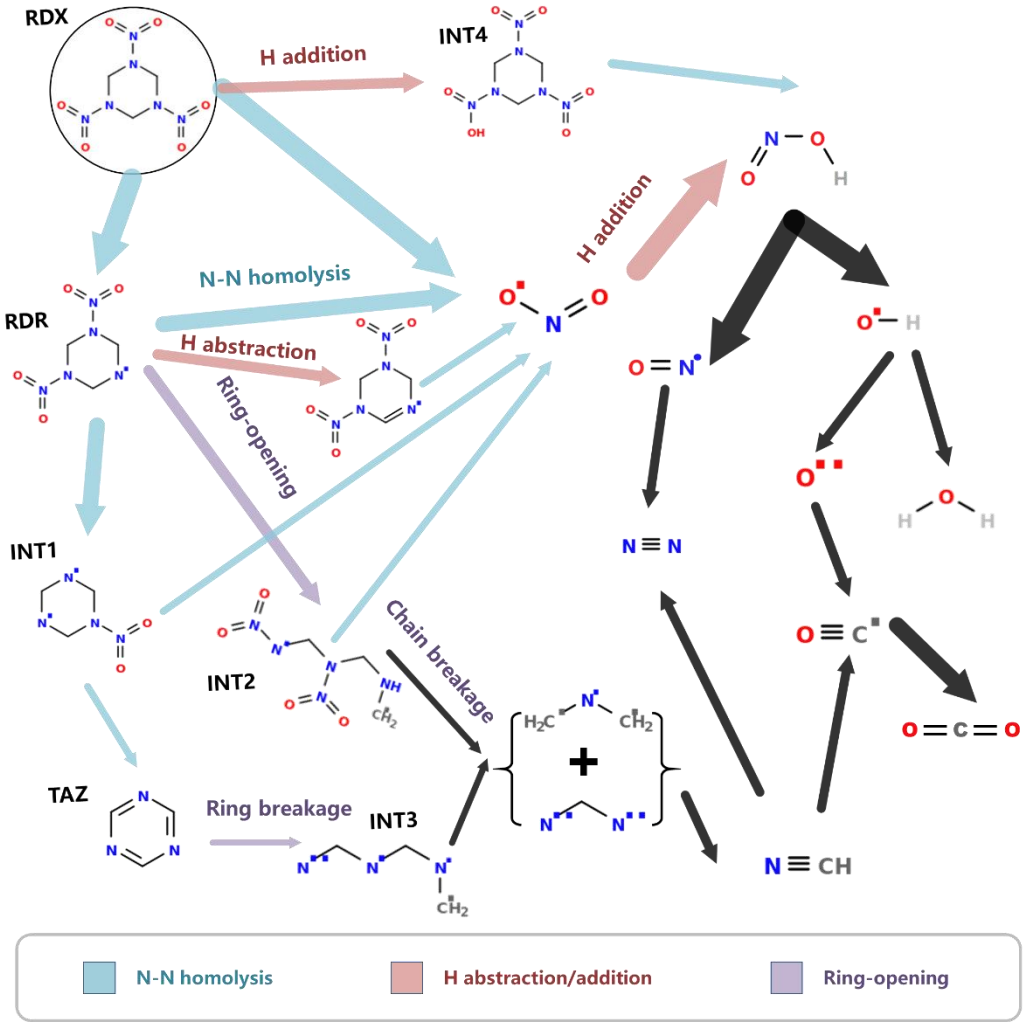

Fig. 8 Primary reaction pathways for the RDX decomposition and the formation of H_2O, CO_2, and N_2. The arrow width represents the observed number of reactions (n), where width = ln (n+1).

In addition, we further perform MD simulations on RDX in the gas phase using NNP, where the densities are selected as 0.5 and 0.1 g/cm^3. The simulations are performed under an NVT ensemble at 2500 K. The results from RDX crystals (1.8 g/cm^3) are also included for comparison. Figure 9 shows the flux of N-N homolysis, H abstraction, and ring-opening reactions of RDX and RDR molecules. As discussed above, RDX crystals are mainly consumed through the N-N homolysis, while the proportion of H abstraction and ring-opening reaction increase for RDR molecules. As the density decreases, the proportion of ring-opening reaction increases significantly (from 6% to 26% for RDX, 17% to 34% for RDR). The proportion of N-N homolysis, and H abstraction reactions decrease with the system density. Such behaviors are attributed to the effects of neighbor molecules. At high-density conditions, the ring-opening reaction is hindered by the neighbor molecules due to the steric effects. Decreasing the density, RDX decomposition is less affected by the neighbor molecule, which is close to the isolated molecule in the previous DFT study[39]. In summary, the effect of the neighbor molecule should be taken into consideration when studying the reaction mechanism of RDX and other EM in the condensed phase in practice.

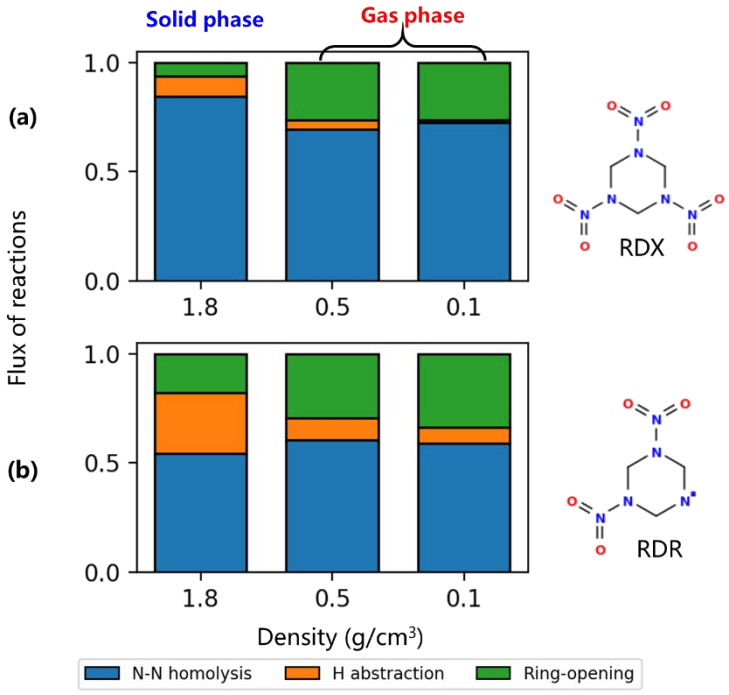

Fig. 9 Flux analysis of N-N homolysis, H abstraction, and ring-opening reactions for the (a) RDX and (b) RDR molecules with densities of 1.8, 0.5, 0.1 g/cm^3.

4. Conclusions

In this work, we develop a neural network-based model to explore the reaction mechanism of RDX with good accuracy. NN-based molecular dynamics simulations of bulk RDX crystals are performed to investigate the mechanism of RDX decomposition. The physical properties of RDX crystal are firstly calculated to validate the accuracy of NN potential, and then the detailed species evolutions are compared with AIMD simulation. Finally, large-scale NN MDs are performed to derive the decomposition reaction mechanism of bulk RDX crystal. The detailed decomposition mechanism is investigated with our NN model. We find that the intermediate and products in the simulations agree well with the TG-FTIR experiments. The RDX decomposition can be divided into two stages. The N-N homolysis dominates the first stage to form NO_2, followed by H abstraction reactions, and produces NO and H_2O. The second stage refers to the ring-opening of large fragments and subsequent chain breakage reactions, forming the final products as N_2 and CO_2.

The present work develops a NN model for RDX at the level of *ab initio* calculations. Our NN model considers both atomic energy and force information from high-level DFT calculations. We demonstrate the accuracy of our NNP outperforms the widely used ReaxFF model. In particular, the ReaxFF model predicts unphysical atomic force compared to DFT calculations. This issue makes it unsuitable for the exploration of the processes in the reaction dynamics. Our NN model also exhibits a great computational efficiency, which is 10000 times faster than the DFT method, and 27 times faster than the ReaxFF method, allowing the possibility of

investigating the complex reaction process of bulk RDX crystal from an atomic perspective. Thus, this study opens new opportunities for complex reactive systems to build reaction kinetics models.

Acknowledgments

This work is supported by the State Key Laboratory of Explosion Science and Technology (Grant ZDKT21-01) and the National Natural Science Foundation of China (Grant 52106130). The authors also acknowledge the support from the Foundation of Science and Technology on Combustion and Explosion Laboratory.

Supplementary material

Fig. S1 Evolution of the major species (RDX, NO_2, NO, H_2O) during the initial stage of RDX decomposition process predicted by AIMD, DP, and ReaxFF models.

References

(1) Song, S.; Tian, X.; Wang, Y.; Qi, X.; Zhang, Q. Theoretical Insight into Density and Stability Differences of RDX, HMX and CL-20. *CrystEngComm* **2022**, *24* (8), 1537–1545. https://doi.org/10.1039/D1CE01577J.

(2) Yan, Q.-L.; Zhao, F.-Q.; Kuo, K. K.; Zhang, X.-H.; Zeman, S.; DeLuca, L. T. Catalytic Effects of Nano Additives on Decomposition and Combustion of RDX-, HMX-, and AP-Based Energetic Compositions. *Prog. Energy Combust. Sci.* **2016**, *57*, 75–136. https://doi.org/10.1016/j.pecs.2016.08.002.

(3) Kuo, K. K. *Fundamentals of Solid-Propellant Combustion*; American Institute of Aeronautics and Astronautics, 1984.

(4) Wight, C. A.; Botcher, T. R. Thermal Decomposition of Solid RDX Begins with Nitrogen-Nitrogen Bond Scission. *J. Am. Chem. Soc.* **1992**, *114* (21), 8303–8304. https://doi.org/10.1021/ja00047a059.

(5) Zhao, X.; Hintsa, E. J.; Lee, Y. T. Infrared Multiphoton Dissociation of RDX in a Molecular Beam. *J. Chem. Phys.* **1988**, *88* (2), 801–810. https://doi.org/10.1063/1.454158.

(6) Khichar, M.; Patidar, L.; Thynell, S. Comparative Analysis of Vaporization and Thermal Decomposition of Cyclotrimethylenetrinitramine (RDX). *J. Propuls. Power* **2019**, *35* (6), 1098–1107. https://doi.org/10.2514/1.B37643.

(7) Yan, Z.; Song, C.; Li, Q.; Niu, Y.; Wang, J.; Huang, Z. A Study on the Effect of Initial Temperature on Combustion Characteristics of RDX Based on the Optical Diagnosis Methods. *Energies* **2022**, *15* (7), 2421. https://doi.org/10.3390/en15072421.

(8) Melius, C. F. Thermochemical Modeling: II. Application to Ignition and Combustion of Energetic Materials. In *Chemistry and physics of energetic materials*; Springer, 1990; pp 51–78.

(9) Harris, N. J.; Lammertsma, K. Ab Initio Density Functional Computations of Conformations and Bond Dissociation Energies for Hexahydro-1,3,5-Trinitro-1,3,5-Triazine. *J. Am. Chem. Soc.* **1997**, *119* (28), 6583–6589. https://doi.org/10.1021/ja970392i.

(10) Patidar, L.; Thynell, S. T. Quantum Mechanics Investigation of Initial Reaction Pathways and Early Ring-Opening Reactions in Thermal Decomposition of Liquid-Phase RDX. *Combust. Flame* **2017**, *178*, 7–20. https://doi.org/10.1016/j.combustflame.2016.12.024.

(11) Zhang, Z.; Ye, L.; Wang, X.; Wu, X.; Gao, W.; Li, J.; Bi, M. Unraveling the Reaction Mechanism on Pyrolysis of 1,3,5-Trinitro-1,3,5-Triazinane (RDX). *Combust. Flame* **2022**, *242*, 112220. https://doi.org/10.1016/j.combustflame.2022.112220.

(12) Wu, X.; Liu, Z.; Zhu, W. Coupling Effect of High Temperature and Pressure on the Decomposition Mechanism of Crystalline HMX. *Energ. Mater. Front.* **2020**, *1* (2), 90–94. https://doi.org/10.1016/j.enmf.2020.08.003.

(13) Zhang, T.; Cheng, L.; Zhang, J.; Wang, K. CPMD Investigation of α-RDX and ε-CL-20: The Transition of Deflagration to Detonation Depending on the Self-Produced Radicals. *Phys Chem Chem Phys* **2020**, *22* (14), 7421–7429. https://doi.org/10.1039/D0CP00050G.

(14) Ji, J.; Wang, K.; Zhu, S.; Zhu, W. Structure, Intermolecular Interactions, and Dynamic Properties of NTO Crystals with Impurity Defects: A Computational Study. *CrystEngComm* **2021**, *23* (12), 2455–2468. https://doi.org/10.1039/D0CE01670E.

(15) Chenoweth, K.; Van Duin, A. C.; Goddard, W. A. ReaxFF Reactive Force Field for Molecular Dynamics Simulations of Hydrocarbon Oxidation. *J. Phys. Chem. A* **2008**, *112* (5), 1040–1053.

(16) Senftle, T. P.; Hong, S.; Islam, M. M.; Kylasa, S. B.; Zheng, Y.; Shin, Y. K.; Junkermeier, C.; Engel-Herbert, R.; Janik, M. J.; Aktulga, H. M.; others. The ReaxFF Reactive Force-Field: Development, Applications and Future Directions. *Npj Comput. Mater.* **2016**, *2* (1), 1–14.

(17) Xiao, Y.; Dong, W.; Busnengo, H. Reactive Force Fields for Surface Chemical Reactions: A Case Study with Hydrogen Dissociation on Pd Surfaces. *J. Chem. Phys.* **2010**, *132* (1), 014704.

(18) Senftle, T. P.; Hong, S.; Islam, M. M.; Kylasa, S. B.; Zheng, Y.; Shin, Y. K.; Junkermeier, C.; Engel-Herbert, R.; Janik, M. J.; Aktulga, H. M.; others. The ReaxFF Reactive Force-Field: Development, Applications and Future Directions. *Npj Comput. Mater.* **2016**, *2* (1), 1–14.

(19) Zuo, Y.; Chen, C.; Li, X.; Deng, Z.; Chen, Y.; Behler, J.; Csányi, G.; Shapeev, A. V.; Thompson, A. P.; Wood, M. A.; Ong, S. P. Performance and Cost Assessment of Machine Learning Interatomic Potentials. *J. Phys. Chem. A* **2020**, *124* (4), 731–745. https://doi.org/10.1021/acs.jpca.9b08723.

(20) Zhang, L.; Han, J.; Wang, H.; Saidi, W.; Car, R.; E, W. End-to-End Symmetry Preserving Inter-Atomic Potential Energy Model for Finite and Extended Systems. In *Advances in Neural Information Processing Systems*; Curran Associates, Inc., 2018; Vol. 31.

(21) Chmiela, S.; Tkatchenko, A.; Sauceda, H. E.; Poltavsky, I.; Schütt, K. T.; Müller, K.-R. Machine Learning of Accurate Energy-Conserving Molecular Force Fields. *Sci. Adv.* **2017**, *3* (5), e1603015. https://doi.org/10.1126/sciadv.1603015.

(22) Cao, L.; Zeng, J.; Wang, B.; Zhu, T.; Zhang, J. Z. H. Ab Initio Neural Network MD Simulation of Thermal Decomposition of a High Energy Material CL-20/TNT. *Phys Chem Chem Phys* **2022**, *24* (19), 11801–11811. https://doi.org/10.1039/D2CP00710J.

(23) Harmeling, S.; Ziehe, A.; Kawanabe, M.; Müller, K.-R. Kernel-Based Nonlinear Blind Source Separation. *Neural Comput.* **2003**, *15* (5), 1089–1124.

(24) Keith, J. A.; Vassilev-Galindo, V.; Cheng, B.; Chmiela, S.; Gastegger, M.; Müller, K.-R.; Tkatchenko, A. Combining Machine Learning and Computational Chemistry for Predictive Insights Into Chemical Systems. *Chem. Rev.* **2021**, acs.chemrev.1c00107. https://doi.org/10.1021/acs.chemrev.1c00107.

(25) Musil, F.; Grisafi, A.; Bartók, A. P.; Ortner, C.; Csányi, G.; Ceriotti, M. Physics-Inspired Structural Representations for Molecules and Materials. *Chem. Rev.* **2021**, *121* (16), 9759–9815. https://doi.org/10.1021/acs.chemrev.1c00021.

(26) Chu, Q.; Luo, K. H.; Chen, D. Exploring Complex Reaction Networks Using Neural Network-Based Molecular Dynamics Simulation. *J. Phys. Chem. Lett.* **2022**, *13*, 4052–4057.

(27) van Duin, A. C. T.; Dasgupta, S.; Lorant, F.; Goddard, W. A. ReaxFF: A Reactive Force Field for Hydrocarbons. *J. Phys. Chem. A* **2001**, *105* (41), 9396–9409. https://doi.org/10.1021/jp004368u.

(28) Liu, L.; Liu, Y.; Zybin, S. V.; Sun, H.; Goddard, W. A. ReaxFF-Lg: Correction of the ReaxFF Reactive Force Field for London Dispersion, with Applications to the Equations of State for Energetic Materials. *J. Phys. Chem. A* **2011**, 7.

(29) Lippert, G.; Hutter, J.; Parrinello, M. The Gaussian and Augmented-Plane-Wave Density Functional Method for Ab Initio Molecular Dynamics Simulations. *Theor. Chem. Acc.* **1999**, *103* (2), 124–140.

(30) Goedecker, S.; Teter, M.; Hutter, J. Separable Dual-Space Gaussian Pseudopotentials. *Phys. Rev. B* **1996**, *54* (3), 1703.

(31) Perdew, J. P.; Burke, K.; Ernzerhof, M. Generalized Gradient Approximation Made Simple. *Phys. Rev. Lett.* **1996**, *77* (18), 3865.

(32) Grimme, S.; Antony, J.; Ehrlich, S.; Krieg, H. A Consistent and Accurate Ab Initio Parametrization of Density Functional Dispersion Correction (DFT-D) for the 94 Elements H-Pu. *J. Chem. Phys.* **2010**, *132* (15), 154104.

(33) VandeVondele, J.; Hutter, J. Gaussian Basis Sets for Accurate Calculations on Molecular Systems in Gas and Condensed Phases. *J. Chem. Phys.* **2007**, *127* (11), 114105.

(34) Zhang, Y.; Wang, H.; Chen, W.; Zeng, J.; Zhang, L.; Wang, H.; E, W. DP-GEN: A Concurrent Learning Platform for the Generation of Reliable Deep Learning Based Potential Energy Models. *Comput. Phys. Commun.* **2020**, 107206. https://doi.org/10.1016/j.cpc.2020.107206.

(35) Zeng, J.; Cao, L.; Chin, C.-H.; Ren, H.; Zhang, J. Z. H.; Zhu, T. ReacNetGenerator: An Automatic Reaction Network Generator for Reactive Molecular Dynamics Simulations. *Phys. Chem. Chem. Phys.* **2020**, *22* (2), 683–691. https://doi.org/10.1039/C9CP05091D.

(36) Chu, Q.; Wang, C.; Chen, D. Towards Fully Ab Initio Modeling of Soot Formation in a Nanoreactor. ChemRxiv 2022. https://doi.org/10.26434/chemrxiv-2022-xfv0x.

(37) Choi, C. S.; Prince, E. The Crystal Structure of Cyclotrimethylenetrinitramine. *Acta Crystallogr. B* **1972**, *28* (9), 2857–2862. https://doi.org/10.1107/S0567740872007046.

(38) Rogers, R.; Smith, L. Application of Scanning Calorimetry to the Study of Chemical Kinetics. *Thermochim. Acta* **1970**, *1* (1), 1–9.

(39) Chakraborty, D.; Muller, R. P.; Dasgupta, S.; Goddard, W. A. The Mechanism for Unimolecular Decomposition of RDX (1,3,5-Trinitro-1,3,5-Triazine), an Ab Initio Study. *J. Phys. Chem. A* **2000**, *104* (11), 2261–2272. https://doi.org/10.1021/jp9936953.

(40) Khichar, M.; Patidar, L.; Thynell, S. T. Improvement and Validation of a Detailed Reaction Mechanism for Thermal Decomposition of RDX in Liquid Phase. *Combust. Flame* **2018**, *198*, 455–465. https://doi.org/10.1016/j.combustflame.2018.10.005.

(41) Ornellas, 15 DL. *Calorimetric Determinations of the Heat and Products of Detonation for Explosives: October 1961 to April 1982*; CALIFORNIA UNIV BERKELEY LAWRENCE LIVERMORE LAB, 1982.

(42) Yoo, P.; Sakano, M.; Desai, S.; Islam, M. M.; Liao, P.; Strachan, A. Neural Network Reactive Force Field for C, H, N, and O Systems. *Npj Comput. Mater.* **2021**, *7* (1), 9. https://doi.org/10.1038/s41524-020-00484-3.